

Cite this: *Polym. Chem.*, 2026, **17**, 1028

# A transfer learning framework integrating molecular dynamics and group contribution methods for predicting polymer specific heat capacity

Sobin Alosious, <sup>a,b</sup> Jiaxin Xu, <sup>b</sup> Meng Jiang <sup>a,c</sup> and Tengfei Luo <sup>\*a,b,d</sup>

Heat capacity ( $C_p$ ) of polymers is an essential property for diverse applications, such as energy storage systems, electronics thermal management, and thermal insulation. In this study, we explore a transfer learning framework to predict polymer  $C_p$ , where models are first pretrained on large datasets generated from molecular dynamics (MD) simulations and group contribution (GC) calculations, and then fine-tuned using experimental data. We evaluate multiple machine learning (ML) models, including multilayer perceptrons and graph neural networks, using various molecular fingerprints and structural descriptors. The trained models are applied to existing polymers and virtual polymers to enable large-scale  $C_p$  prediction and screening. We analyze structure–property relationships to identify key molecular features influencing  $C_p$  and propose an updated GC model through a data-driven regression for quick  $C_p$  evaluation. Using the predicted  $C_p$ , in combination with thermal conductivity and glass transition temperature, we search polymers for four functional categories relevant to thermal applications: thermal interface materials, insulators, buffers, and heat spreaders. Representative polymer candidates are identified for each category based on the combined thermal property thresholds, demonstrating the practical relevance of predicted values for real-world material selection. This integrated approach enables targeted selection of polymer materials for specific thermal applications.

Received 3rd November 2025,  
Accepted 3rd February 2026

DOI: 10.1039/d5py01039j

rsc.li/polymers

## Introduction

Efficient thermal energy management is increasingly critical across various sectors, including industry, electronics, and transportation, to enhance energy efficiency, reduce carbon emissions, and ensure system reliability.<sup>1–4</sup> A significant portion of industrial energy input is typically lost as waste heat. Integrating waste heat recovery with thermal energy storage technologies offers the potential to capture and repurpose this otherwise wasted energy, contributing to more efficient energy practices.<sup>5</sup> In electronics, overheating remains a primary cause of component failures, underscoring the importance of implementing robust thermal management

strategies to maintain device performance and longevity.<sup>6</sup> In electric vehicles, battery performance and safety are susceptible to temperature control.<sup>7</sup> Latent heat thermal energy storage systems, which utilize phase change materials, offer an effective means of storing and releasing thermal energy.<sup>8</sup>

For diverse applications, a comprehensive evaluation of thermal properties, particularly thermal conductivity (TC) and specific heat capacity ( $C_p$ ), is therefore vital. While extensive research has focused on enhancing TC to improve heat transfer efficiency,<sup>9–13</sup>  $C_p$  is equally important because it governs a material's ability to store thermal energy. Polymers have emerged as desirable candidates for thermal energy storage and management because of their unique combination of practical advantages, including low cost, lightweight, mechanical flexibility, and ease of processing into various shapes for scalable manufacturing and integration, while also offering high corrosion resistance and inherent electrical insulation.<sup>14–19</sup>

Various approaches exist for determining polymer  $C_p$ , including experimental methods, molecular dynamics (MD) simulations, group contribution (GC) techniques, and machine learning (ML) models. Experimental techniques, such as differential scanning calorimetry (DSC), provide direct

<sup>a</sup>Lucy Family Institute for Data and Society, University of Notre Dame, Notre Dame, IN, 46556, USA. E-mail: tluo@nd.edu<sup>b</sup>Department of Aerospace and Mechanical Engineering, University of Notre Dame, Notre Dame, IN, 46556, USA<sup>c</sup>Department of Computer Science and Engineering, University of Notre Dame, Notre Dame, IN, 46556, USA<sup>d</sup>Department of Chemical and Biomolecular Engineering, University of Notre Dame, Notre Dame, IN, 46556, USA

and accurate measurements.<sup>20</sup> However, they are time-consuming and require significant sample preparation and calibration. MD simulations provide atomistic insights and can handle a wide range of temperatures and polymer architectures,<sup>21</sup> but classical MD tends to overpredict  $C_p$  as quantum effects are not accounted for.<sup>22</sup> GC methods estimate  $C_p$  based on additive contributions of functional groups and are computationally efficient and suitable for large datasets, but their accuracy diminishes for complex polymers with intricate structures or interactions.<sup>23</sup> Recently, ML models have shown great promise in predicting  $C_p$  by learning from experimental and simulation data, offering rapid predictions and the ability to generalize across diverse polymer chemistries.<sup>24</sup> However, they require large, high-quality datasets, and careful feature engineering to avoid overfitting. Overall, integrating these methods may enable cross-validation and a balanced assessment of polymer  $C_p$ .

Recent advances in polymer informatics have further expanded the potential of ML in this field.<sup>19,25</sup> For example, Bhowmik *et al.*<sup>24</sup> applied Decision Tree (DT) and Principal Component Analysis (PCA) models to predict room-temperature  $C_p$  values for 68 polymers using experimentally derived molecular descriptors. Despite the limited dataset size, their optimized DT model achieved testing  $R^2$  values up to 0.83 under 5-fold cross-validation, demonstrating that physically meaningful polymer descriptors can capture key structure –  $C_p$  relationships. Their analysis further highlighted the dominant role of bonding, molecular-type, and atom-type descriptors in governing polymer heat capacity, illustrating the potential of ML for guiding polymer design even in data-scarce regimes. Building on this, Hayashi *et al.*<sup>26</sup> applied a transfer learning (TL) strategy to bridge discrepancies between MD-calculated and experimental polymer properties, including  $C_p$ , linear expansion coefficient, and volume expansion coefficient. Using MD-derived data as a source domain and fine-tuning neural networks on limited experimental data from PoLyInfo, they substantially reduced systematic bias in  $C_p$  predictions. Specifically, while direct MD calculations exhibited large errors (RMSE  $\approx 1972 \text{ J kg}^{-1} \text{ K}^{-1}$ ), transfer learning reduced the RMSE to approximately  $279 \text{ J kg}^{-1} \text{ K}^{-1}$ , corresponding to an error reduction of nearly 85% relative to raw MD predictions. These results demonstrate the effectiveness of TL in correcting MD-induced biases and highlight its utility for polymer thermo-physical property prediction when experimental data are scarce. Furthermore, Malashin *et al.*<sup>27</sup> explored a wide range of ML approaches for predicting various physical properties of polymers, including  $C_p$ . Utilizing a comprehensive polymer dataset, they compared ensemble, tree-based, regularization, and distance-based regression models. While their random forest models achieved  $R^2$  values up to 0.88 for certain thermal properties, the performance on  $C_p$  prediction was notably lower ( $R^2 \approx 0.13$ ). This highlights both the potential of ML to capture complex polymer behaviors and the challenges of accurately modeling specific properties such as heat capacity, emphasizing the importance of careful model selection and the need for improved feature representations.

In this study, we present a comprehensive TL framework for accurate and scalable predictions of  $C_p$  in polymers. The TL strategy integrates multiple data fidelities, including (1) low-fidelity GC predictions derived from functional group analysis and MD simulations and (2) high-fidelity experimental data. We first develop extensive GC and MD datasets through automated workflows, including polymer system construction, equilibration, and  $C_p$  calculation. ML models such as Multilayer Perceptrons (MLP) and Graph Neural Networks (GNNs) are pretrained on GC or MD data and subsequently fine-tuned with limited experimental data using TL, leading to improved performance compared to models trained on experimental data alone. We also explore large language models (LLMs) with advanced prompting strategies to complement structure-based ML approaches. By leveraging the predictive power of TL-enhanced models, we identify polymers suitable for various thermal management applications by combining  $C_p$  predictions with thermal conductivity (TC) data from our previous studies. Finally, we develop a data-driven GC model and analyze key structural and physicochemical factors that govern  $C_p$ , providing both interpretability and physical insights. The primary novelty of this work lies in the unified multi-fidelity TL framework, large-scale  $C_p$  prediction across real and virtual polymer spaces, and systematic benchmarking of specialized ML and LLM-based approaches. The GC refitting and application-oriented categorization are presented as complementary, enabling components that enhance interpretability and demonstrate practical use of the predicted properties.

## Methodology

### Molecular dynamics simulations

To compute  $C_p$  of amorphous polymers, we employed a high-throughput MD pipeline consisting of polymer model generation, equilibration, and  $C_p$  calculation using both equilibrium and non-equilibrium approaches. The polymer generation and equilibration stages were adapted from our previous work.<sup>13,28</sup> An overview of the MD workflow is illustrated schematically in Fig. 1.

Polymer monomers were represented by simplified molecular input line entry system (SMILES) strings.<sup>29</sup> A Python-based pipeline built on PYSIMM<sup>30</sup> was used to create the initial structure of amorphous polymers. This process involves generating a polymer chain for each constituent polymer through polymerization, with each chain containing approximately 600 atoms. Force field parameters were assigned using the General AMBER Force Field 2 (GAFF2),<sup>31</sup> with partial atomic charges assigned using the Gasteiger method. No quantum-chemical charge derivation (*e.g.*, AM1-BCC or RESP) was performed, and charges were not refitted after polymerization; instead, Gasteiger charges were assigned automatically and consistently to all polymerized structures to enable scalable high-throughput simulations. GAFF2 is widely used for calculation of thermophysical properties in polymers due to its

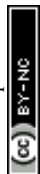




Fig. 1 Schematic workflow illustrating the process from polymer SMILES input to  $C_p$  prediction via MD simulations and GC methods, followed by TL using experimental data.

broad chemical coverage and established parameterization.<sup>26,32,33</sup> To assess the sensitivity of MD-derived  $C_p$  to force-field choice, a targeted comparison was performed between GAFF2-GAFF and GAFF2-CHARMM using identical simulation protocols. The GAFF2-GAFF comparison yields a mean absolute percentage deviation (MAPE) of 4.8% (95% of deviations below 17.3%), while the GAFF2-CHARMM comparison exhibits a MAPE of 14.5% (95% of deviations below ~32.8%), indicating bounded but force-field-dependent uncertainty. Parity plots illustrating these comparisons are shown in Fig. 2(a) and (b). These results support the use of GAFF2-based MD data as a low-fidelity input within the multi-fidelity learning framework rather than assuming force-field invariance. Each polymer chain was duplicated to form a six-chain system, which was placed in a simulation box with periodic boundary conditions in all spatial directions. Input scripts compatible with large-scale atomic-molecular massively parallel simulator (LAMMPS)<sup>34</sup> were generated automatically by the python pipeline for subsequent simulations. After initialization, the system undergoes multiple optimization steps, which are broadly classified into two stages: initial relaxation and annealing.

**Initial relaxation.** Electrostatic interactions were turned off, and Lennard-Jones (LJ) interactions were truncated at a cutoff distance of 0.3 nm to avoid large forces from long-range interactions during the initial relaxation of the randomly packed system. The system was first equilibrated under an NPT ensemble at 100 K for 2 ps using a 0.1 fs time step. This was followed by heating from 100 K to 1000 K over 1 ns under the NVT ensemble. Subsequently, the system was equilibrated at 1000 K and 0.1 atm for 50 ps in the NPT ensemble, and then for 1 ns in the NPT ensemble while ramping the pressure from 0.1 atm to 500 atm

using a 1 fs time step. SHAKE<sup>35</sup> constraints were applied to maintain covalent bond lengths and ensure numerical stability.

**Annealing.** During this stage, electrostatic interactions were re-enabled using the particle-particle-particle-mesh (PPPM)<sup>36</sup> Ewald summation method, and the LJ cutoff was increased to 0.800 nm. The system was equilibrated under an NPT ensemble at 1000 K and 1 atm for 2 ps with a 0.1 fs time step, then cooled to 300 K at a rate of 140 K ns<sup>-1</sup> with SHAKE constraints. A final NPT simulation was conducted at 300 K and 1 atm for 8 ns using a 1 fs time step to achieve a stable amorphous configuration.

**Equilibrium MD (EMD).** After equilibration, the system was simulated under NPT ensemble at 300 K and 1 atm for 10 ns to ensure statistically meaningful sampling of thermodynamic fluctuations. During this production run, the instantaneous enthalpy of the system was recorded at regular time intervals. The  $C_p$  was calculated using the fluctuation-dissipation theorem,<sup>37</sup> which relates macroscopic thermodynamic response functions to microscopic energy fluctuations:

$$C_p = \frac{\langle H^2 \rangle - \langle H \rangle^2}{k_B T^2}, \quad (1)$$

where  $H$  is the system enthalpy,  $T$  is the absolute temperature, and  $k_B$  is Boltzmann's constant. The angle brackets represent ensemble averages. This approach assumes the system is fully equilibrated and follows canonical ensemble statistics, and it has been widely used to estimate  $C_p$  in liquids, solids, and polymeric materials.<sup>37,38</sup>

**Non-equilibrium MD (NEMD).** In addition to the fluctuation-based approach, we employed a direct method to estimate  $C_p$  based on the enthalpy-temperature relationship.



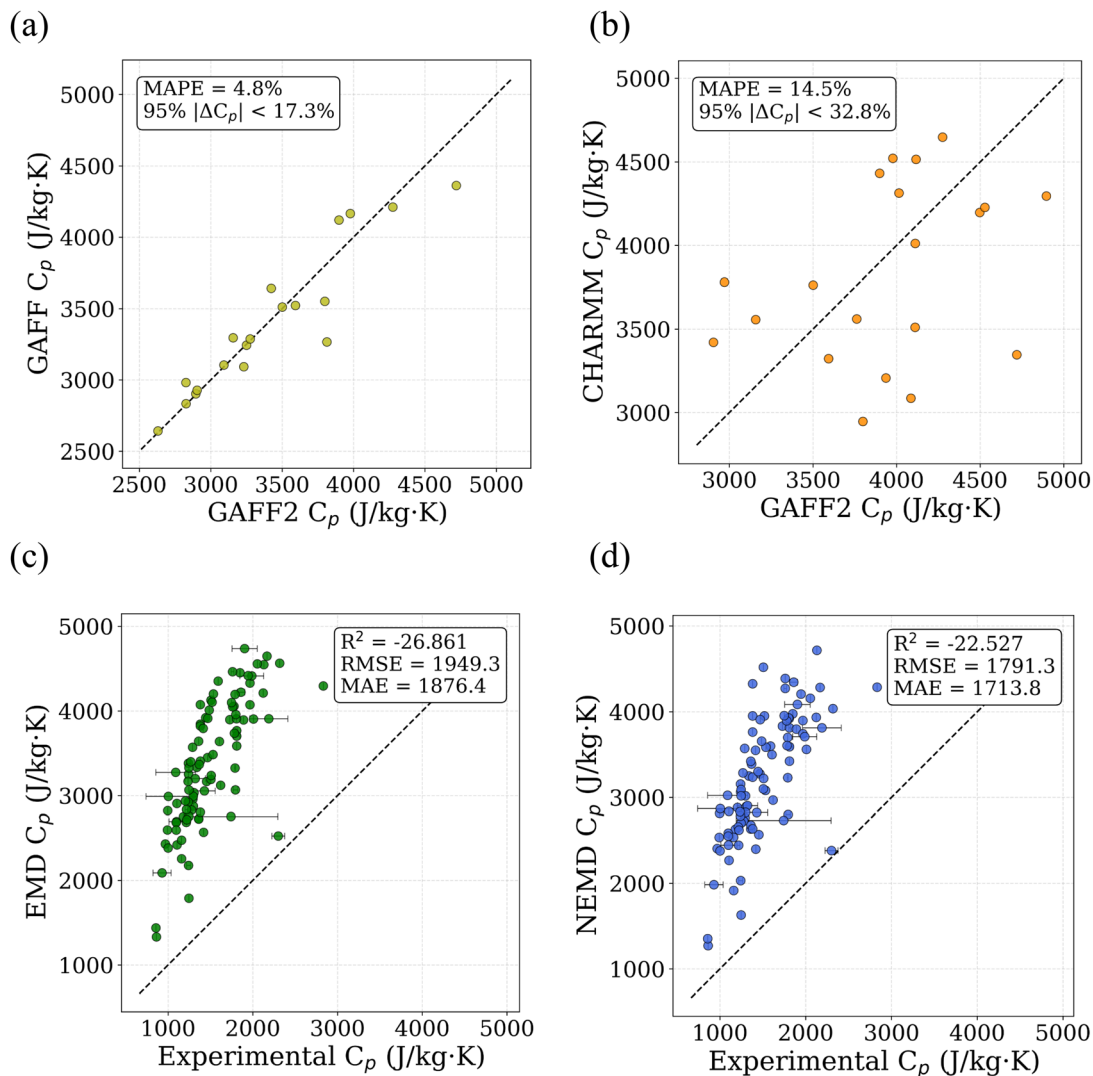


Fig. 2 (a) Comparison between  $C_p$  calculated using GAFF2 and GAFF force fields. (b) Comparison between  $C_p$  calculated using GAFF2 and CHARMM force fields. (c) Comparison between EMD-predicted and experimental  $C_p$  values. (d) Comparison between NEMD-predicted and experimental  $C_p$  values.

Initially, the system was equilibrated at 290 K and 1 atm for 2 ns. The equilibrated system was gradually heated from 290 K to 310 K over 10 ns under NPT conditions to simulate a controlled temperature ramp. This range was centered around 300 K, the target temperature for  $C_p$  evaluation. At regular intervals, the average enthalpy and temperature of the system were computed and an enthalpy–temperature curve was plotted.  $C_p$  was then calculated as the slope of a linear fit to the enthalpy–temperature curve:<sup>21</sup>

$$C_p = \left( \frac{dH}{dT} \right)_p \quad (2)$$

**EMD vs. NEMD comparison.** Both EMD- and NEMD-based approaches were evaluated for estimating polymer  $C_p$  using the same set of representative systems. In both cases, large deviations from experimental  $C_p$  were observed, consistent

with the known limitations of classical force fields in capturing quantum vibrational contributions. For EMD, the resulting errors are  $RMSE \approx 1950 \text{ J kg}^{-1} \text{ K}^{-1}$  and  $MAE \approx 1876 \text{ J kg}^{-1} \text{ K}^{-1}$ , whereas NEMD yields lower errors, with  $RMSE \approx 1791 \text{ J kg}^{-1} \text{ K}^{-1}$  and  $MAE \approx 1713 \text{ J kg}^{-1} \text{ K}^{-1}$ , indicating improved numerical stability and reduced sensitivity to enthalpy fluctuation noise. Parity plots comparing EMD and NEMD predictions against experimental values are shown in Fig. 2(c) and (d), respectively. Based on this comparison, NEMD was selected as the MD approach used throughout this work to generate low-fidelity  $C_p$  data, which are treated strictly as approximate inputs for subsequent TL analyses.

### Group contribution method

The GC method is a well-established approach for estimating thermophysical properties of molecules by assuming that the total property is an additive function of the contributions from



individual structural groups.<sup>39</sup> For  $C_p$  calculations, the property of a polymer repeat unit is expressed as the weighted sum of predefined group contributions:

$$C_p = \sum_{i=1}^N n_i \cdot G_i, \quad (3)$$

where  $n_i$  is the number of occurrences of the  $i$ -th functional group in the repeat unit,  $G_i$  is the specific heat contribution of that group, and  $N$  is the total number of functional groups considered.

In this work, we used a set of 32 predefined functional groups, and their corresponding  $C_p$  contribution values adopted from the literature.<sup>39</sup> A Python-based workflow was developed using RDKit<sup>40</sup> to parse each SMILES string, identify all matching functional groups in the monomer, and count their occurrences. Once the group counts were determined, each polymer's  $C_p$  was calculated as a linear combination of the group contributions using eqn (3). This method provides a rapid, structure-based estimation of  $C_p$  and serves as a complementary baseline to MD simulations and ML models. An overview of the GC-based property prediction workflow is illustrated in Fig. 1.

### Machine learning framework

**Polymer representation.** To represent polymer structures for ML, SMILES strings were transformed into a set of complementary molecular fingerprints capturing local chemistry, connectivity, and topological features. Multiple fingerprinting schemes were employed to ensure robustness with respect to molecular representation rather than reliance on a single descriptor type. Specifically, we used circular **Morgan** fingerprints (radius = 2, 2048 bits) to encode local atomic environments, **MACCS** keys (166 bits) to capture standardized functional group motifs, and **RDKit** topological fingerprints (2048 bits, path lengths 1–6) to represent path-based connectivity patterns. In addition, **atom pair** and **topological torsion** fingerprints (both 2048 bits) were included to encode long-range atom–atom relationships and torsional connectivity, respectively. Finally, **polymer embedding** fingerprints were obtained from pretrained unsupervised models trained on the PI1M dataset, yielding dense representations that capture broader structural and physicochemical similarities among polymers.<sup>41</sup>

**Model architectures and training strategy.** We employed three classes of ML models to benchmark polymer  $C_p$  prediction: multilayer perceptrons (MLPs), graph neural networks (GNNs), and graph rationalization with environment-based augmentations (GREA). Together, these models span fixed-length descriptor-based learning, graph-based learning, and interpretable rationale-driven learning.

**Multilayer perceptron (MLP).** MLP models were implemented using the Keras API with a TensorFlow backend.<sup>42</sup> The architecture consisted of two hidden layers with ReLU activation and dropout regularization, followed by a linear output layer for  $C_p$  prediction. Models were trained using the MSE loss and the Adam optimizer. Key architectural and training hyperpa-

rameters, including hidden-layer size, dropout rate, and learning rate, were optimized using the Optuna framework<sup>43</sup> to ensure fair comparison across representations.

**Graph neural networks (GNNs).** Graph-based models were implemented using the torch-molecule library.<sup>44</sup> We evaluated two widely used architectures, Graph Isomorphism Networks (GIN)<sup>45</sup> and Graph Convolutional Networks (GCN),<sup>46</sup> which differ in expressive power and message-passing formulation. Hyperparameters related to network depth, embedding dimension, normalization strategy, learning rate, and regularization were optimized using Optuna. These choices were guided by dataset size and the requirements of the transfer-learning framework.

**Graph rationalization with environment-based augmentations (GREA).** The GREA model was also implemented using torch-molecule.<sup>44</sup> Unlike conventional GNNs, GREA explicitly identifies graph rationales, *i.e.*, subgraph structures most responsible for property prediction, and augments training with environment-based perturbations. This design improves interpretability and robustness by encouraging the model to focus on chemically meaningful substructures. Hyperparameters governing the graph encoders, embedding dimension, regularization, and rationale size were optimized using Optuna.

**Transfer learning strategy.** To enhance the prediction accuracy of polymer  $C_p$  using limited experimental data, we employed a two-stage TL approach. The philosophy behind transfer learning is that models pretrained on large proxy datasets (*e.g.*, MD or GC results) can capture general structure–property relationships that are also relevant to experimental  $C_p$ . These learned representations provide a strong starting point, such that fine-tuning on limited experimental data does not begin from scratch. All polymers appearing in the experimental dataset are explicitly excluded from the MD and GC datasets prior to pretraining and calibration, ensuring that no experimental information is used during proxy-data training and eliminating any possibility of data leakage. All TL models were evaluated using a nested cross-validation (nested CV) framework. An outer cross-validation loop defines held-out experimental test folds, while an inner cross-validation loop is used exclusively for hyperparameter optimization. In our workflow, models such as MLP, GNN, and GREA were first pretrained on large MD or GC datasets, then fine-tuned on experimental data. For each outer CV fold, pretraining is performed on the proxy dataset after excluding any polymers that appear in the corresponding experimental folds, ensuring strict separation between proxy and experimental data. The pretrained model is then fine-tuned only on the experimental training data of the outer fold, and final performance is evaluated on the held-out experimental test fold. Before fine-tuning, we reset the final predictor layers with Xavier uniform initialization for weights and zero initialization for biases, helping mitigate overfitting and improve adaptation to experimental data. During fine-tuning, the network architecture learned during pretraining is kept fixed, while training-related hyperparameters, including learning rate, batch size, weight decay, and early stopping criteria, are optimized within the inner CV loop.



A reduced learning rate is used during fine-tuning relative to pretraining to promote stable convergence while retaining transferable representations. Hyperparameter tuning was conducted using the Optuna framework, optimizing parameters such as learning rate, dropout ratio, hidden dimensions, and training schedule parameters.

**Reproducibility details.** To enable full reproducibility, we explicitly specify preprocessing, training settings, and the hyperparameter search used for all results in Table 1. Polymers are represented from repeat-unit SMILES using RDKit fingerprints (Morgan radius 2, 2048 bits; MACCS 166 bits; RDKit topological 2048 bits; atom-pair 2048 bits; topological-torsion 2048 bits) and optional seven RDKit descriptors (MolWt, TPSA, NumHDonors, NumHAcceptors, NumRotatableBonds, RingCount, FractionCSP3). Duplicate SMILES in the experimental dataset are consolidated by averaging the target value. Invalid SMILES and any rows with non-finite features/targets are removed. When descriptors are included, input features are standardized using training-set statistics only. All models are evaluated using nested cross-validation (outer: 5 folds; inner: 3 folds). Hyperparameters are optimized exclusively in the inner loop using Optuna (TPE sampler) with validation RMSE as the objective. MLPs are trained with MSE loss using AdamW and early stopping on validation loss. The EXP-only search space includes: number of layers (2–4), hidden width

(128–1024) with shrink factor (0.55–0.95), dropout (0–0.35), learning rate ( $10^{-5}$ – $5 \times 10^{-3}$ ), weight decay ( $10^{-8}$ – $10^{-2}$ ), batch size (16–128), max epochs (80–300), and patience (10–30). For transfer learning, any polymer present in the experimental outer folds is removed from the proxy dataset prior to pretraining. During fine-tuning, architecture is fixed and only training hyperparameters are tuned (learning rate  $10^{-6}$ – $5 \times 10^{-4}$ , weight decay  $10^{-8}$ – $10^{-2}$ , batch size 8–64, max epochs 80–300, patience 10–40); all layers are trainable by default.

### Large language model-based prediction

To qualitatively explore the limits of general-purpose language models for polymer property prediction, we benchmarked several LLMs, including LLaMA 4, Qwen3, GPT-4o, Gemini 2.0 Flash, and Mistral Large, under zero-shot and few-shot in-context learning (ICL) settings. Unlike traditional ML models trained on structured molecular representations, LLMs rely on pretrained linguistic knowledge and contextual examples provided at inference time and do not involve model training or parameter optimization in this study.

LLMs were prompted to predict polymer  $C_p$  values using different molecular representations, including SMILES strings, IUPAC names, and functional group counts. In the zero-shot setting, predictions were generated without examples, whereas

**Table 1** Performance comparison of different models and molecular fingerprints within the TL framework, using MD- and GC-derived datasets for pretraining followed by fine-tuning on experimental data

Model	Fingerprint	MD			GC		
		$R^2$	RMSE	MAE	$R^2$	RMSE	MAE
MLP	AtomPair	0.12 ± 0.37	310.17 ± 26.93	230.56 ± 19.21	<b>0.60 ± 0.18</b>	<b>215.01 ± 54.70</b>	<b>160.64 ± 29.31</b>
	MACCS	0.55 ± 0.12	235.04 ± 65.27	172.66 ± 41.10	0.50 ± 0.09	246.44 ± 64.87	177.73 ± 36.46
	Morgan	0.30 ± 0.10	290.90 ± 62.26	214.14 ± 44.42	0.54 ± 0.18	235.50 ± 80.50	177.30 ± 43.51
	PE	0.55 ± 0.09	236.75 ± 71.41	184.00 ± 42.65	0.56 ± 0.11	234.08 ± 72.59	183.25 ± 37.32
	RDKit	0.21 ± 0.28	298.53 ± 43.91	207.48 ± 35.73	0.57 ± 0.19	224.24 ± 73.76	164.34 ± 49.64
	Topological torsion	0.27 ± 0.36	289.03 ± 107.65	214.99 ± 72.13	0.46 ± 0.20	250.92 ± 80.41	183.30 ± 61.41
MLP + Desc	AtomPair	0.29 ± 0.45	272.26 ± 47.93	222.03 ± 29.20	0.35 ± 0.39	262.28 ± 46.64	208.12 ± 30.26
	MACCS	0.56 ± 0.09	233.29 ± 69.87	180.30 ± 46.80	0.52 ± 0.13	237.90 ± 54.74	179.61 ± 39.20
	Morgan	0.31 ± 0.19	288.05 ± 81.28	216.93 ± 53.45	0.39 ± 0.31	259.55 ± 53.00	183.91 ± 28.21
	PE	<b>0.59 ± 0.17</b>	<b>222.39 ± 56.23</b>	<b>167.70 ± 31.74</b>	0.60 ± 0.18	220.59 ± 87.10	159.85 ± 48.93
	RDKit	0.46 ± 0.22	258.29 ± 98.34	186.01 ± 52.88	0.53 ± 0.16	237.34 ± 67.53	170.17 ± 32.48
	Topological torsion	0.32 ± 0.11	284.02 ± 51.26	208.90 ± 40.43	0.43 ± 0.10	264.64 ± 75.43	184.42 ± 47.60
Polymer-family split	MLP(PE)	0.47 ± 0.25	264.50 ± 57.84	207.60 ± 32.43	0.45 ± 0.29	269.42 ± 56.14	199.93 ± 34.16
GREA	None	0.36 ± 0.25	276.46 ± 60.37	199.08 ± 37.83	0.43 ± 0.16	280.52 ± 63.99	199.04 ± 26.70
	MACCS	0.43 ± 0.15	267.75 ± 68.19	187.78 ± 40.93	0.40 ± 0.23	289.81 ± 97.46	188.82 ± 58.65
	Morgan	0.40 ± 0.13	274.88 ± 65.27	190.25 ± 42.92	0.39 ± 0.22	299.39 ± 77.13	208.49 ± 45.83
	MACCS + Morgan	0.36 ± 0.30	280.74 ± 78.37	192.48 ± 47.25	0.37 ± 0.19	275.89 ± 69.63	194.27 ± 42.57
GNN	None	0.41 ± 0.22	284.32 ± 72.31	193.21 ± 33.40	0.32 ± 0.26	289.65 ± 71.84	187.17 ± 37.74
	MACCS	0.44 ± 0.08	268.28 ± 69.56	187.09 ± 42.27	0.47 ± 0.22	271.54 ± 79.38	190.51 ± 37.52
	Morgan	0.41 ± 0.24	284.00 ± 79.09	192.69 ± 36.79	0.42 ± 0.23	284.16 ± 88.74	192.63 ± 37.19
	MACCS + Morgan	0.37 ± 0.19	282.84 ± 79.39	205.65 ± 53.59	0.43 ± 0.20	268.12 ± 84.31	191.60 ± 57.22
Combined	<b>Combined (MD + GC)</b>						
	<b>Average</b>	<b>0.65 ± 0.18</b>	<b>202.1 ± 61.9</b>	<b>147.4 ± 38.4</b>			
	<b>Best</b>	<b>0.74 ± 0.08</b>	<b>184.28 ± 60.3</b>	<b>119.09 ± 46.4</b>			

The results correspond exclusively to TL models. Metrics are reported as mean ± standard deviation across 5-fold nested cross-validation.



in the few-shot setting, a small number of contextual examples with known  $C_p$  values were included in the prompt.

Few-shot examples were selected using a similarity-based strategy. Each query polymer was represented using a Morgan fingerprint, and Tanimoto similarity<sup>47</sup> was used to identify structurally similar polymers with available experimental  $C_p$  data. The most similar entries were used as in-context examples. Standardized prompts were employed to ensure consistent numerical outputs across models. Because LLMs do not involve training or hyperparameter tuning, prediction accuracy was evaluated using standard 5-fold cross-validation, whereas nested cross-validation was reserved for trainable ML models to control hyperparameter optimization bias.

### Datasets

We primarily make use of three types of datasets: experimental data, and data generated from MD simulations and GC calculations. The high-fidelity experimental  $C_p$  dataset used in this study was manually curated from the PolyInfo database and consists of approximately 120 unique amorphous polymers with  $C_p$  values reported near  $300 \pm 2$  K. After removing duplicate entries and averaging repeated measurements for identical polymers, this dataset represents the full set of reliable experimental  $C_p$  data currently available under consistent thermodynamic conditions. Due to the limited availability of experimental  $C_p$  measurements for polymers, no larger or fully independent external experimental dataset exists at present. The MD dataset includes over 850 polymers whose  $C_p$  values were computed through high-throughput NEMD simulations conducted at 300 K. The details for system preparation, equilibration, and  $C_p$  extraction are provided in the Methodology section. The GC dataset consists of over 10 000 polymers for

which  $C_p$  values were estimated using a GC method based on the additive contributions of 32 functional groups, corresponding to 298.15 K. The procedure for GC-based calculation is also explained in the Methodology section. In addition to these  $C_p$  datasets, we collected SMILES strings for approximately 13 000 real polymers from PolyInfo database<sup>48</sup> and 1 million virtual polymers from the PI1M database,<sup>41</sup> which was generated using a recurrent neural network (RNN) trained on real polymers from the PolyInfo database. These SMILES datasets provide a rich molecular representation of chemical space for virtual screening and prediction tasks. To visualize and compare the  $C_p$  distributions across the three datasets, we employed a violin plot (Fig. 3a), which combines a boxplot with a kernel density estimate to illustrate the full distribution of  $C_p$  values for each data source. The width of each violin indicates the density of data points at different  $C_p$  ranges, while central lines reflect the median and interquartile range. To understand how the molecular structures from each dataset occupy chemical space, we applied t-SNE (t-distributed stochastic neighbor embedding) dimensionality reduction on Morgan fingerprints derived from SMILES strings (Fig. 3b). Each point represents a polymer, and proximity in the 2D plot reflects structural similarity in the high-dimensional fingerprint space.

## Results and discussion

To assess the suitability of GAFF2 for large-scale polymer simulations, we performed an explicit validation by comparing MD-predicted polymer densities with available experimental values (Fig. 4a). The MD densities show good agreement with experi-



**Fig. 3** Distribution and structural comparison of polymer datasets. (a) Violin plot showing the distribution of  $C_p$  values for the experimental ( $N = 120$ ), MD-simulated ( $N = 851$ ), and GC-derived ( $N = 10\,568$ ) datasets. (b) t-SNE visualization of the corresponding chemical space based on Morgan fingerprints, illustrating the structural coverage of each dataset.





**Fig. 4** Parity plots comparing MD and GC predictions with experimental data. (a) Comparison between MD-calculated and experimental polymer densities. (b) Comparison between MD-predicted and experimental  $C_p$  values. (c) Comparison between bias-corrected MD-predicted and experimental  $C_p$  values. (d) Comparison between GC-predicted and experimental  $C_p$  values. Error bars represent the experimental uncertainty in  $C_p$ , quantified as the standard deviation obtained from multiple independently reported experimental  $C_p$  values for the same polymer, with the mean value used for comparison. All  $C_p$  values are evaluated at 300 K.

ment, with an  $R^2$  of 0.50 and low absolute errors, indicating that GAFF2 reasonably captures equilibrium packing and structural properties across a chemically diverse polymer set. While this validation does not imply quantitative accuracy for all thermophysical properties, it supports the use of GAFF2 as a consistent and physically meaningful low-fidelity proxy within the proposed multi-fidelity and TL framework. To evaluate the accuracy of the MD-calculated  $C_p$  values, we compared them with the experimental dataset. Fig. 4b presents the parity plot between MD predictions and experimental values. The plot clearly shows that the MD-calculated (NEMD method)  $C_p$  values are consistently overestimated, as indicated by a high positive mean error (ME) of +1713.79 J (kg K)<sup>-1</sup>. Similar over-

predictions by classical MD methods have been reported in previous studies.<sup>21,26</sup> One fundamental reason for this overestimation lies in the inherent limitations of classical MD simulations, which do not account for quantum mechanical effects. Specifically, the vibrational energy in a classical harmonic oscillator is higher than that in its quantum mechanical counterpart at the same frequency. For high frequency vibrational modes, they are not fully excited at room temperature (300 K) according to the Bose–Einstein distribution. However, in MD simulations, which follows the classical Boltzmann distribution, all modes are fully excited despite the temperature. This discrepancy can be quantitatively described using the expressions for quantum and classical heat



capacities.<sup>49</sup> The quantum heat capacity for a harmonic oscillator is given by:

$$C_{\text{quantum}} = 3Nk_{\text{B}} \left( \frac{\hbar\omega}{k_{\text{B}}T} \right)^2 \frac{e^{\frac{\hbar\omega}{k_{\text{B}}T}}}{\left( e^{\frac{\hbar\omega}{k_{\text{B}}T}} - 1 \right)^2}, \quad (4)$$

while the classical value is:

$$C_{\text{classical}} = 3Nk_{\text{B}}. \quad (5)$$

From eqn (4) and (5), the ratio of the quantum to classical heat capacities can be expressed as:

$$\frac{C_{\text{quantum}}}{C_{\text{classical}}} = \left( \frac{\hbar\omega}{k_{\text{B}}T} \right)^2 \frac{e^{\frac{\hbar\omega}{k_{\text{B}}T}}}{\left( e^{\frac{\hbar\omega}{k_{\text{B}}T}} - 1 \right)^2}. \quad (6)$$

This ratio decreases monotonically with increasing vibrational frequency  $\omega$ , which explains the systematic overestimation of  $C_{\text{p}}$  in classical MD simulations, particularly for polymers with stiff bonds. Previous studies have demonstrated that classical MD systematically overestimates thermophysical properties due to its neglect of quantum effects,<sup>50</sup> and that the deviation between MD-predicted and experimental  $C_{\text{p}}$  values increases with the average bond-stretching and -bending force constants.<sup>26</sup> Despite this systematic bias, the strong correlation between MD and experimental results suggests that the discrepancy may be addressed using data-driven correction strategies, such as TL or multi-fidelity modeling. We examined differences between MD-predicted and experimental  $C_{\text{p}}$  values across different polymer classes and structural motifs. However, only a small number of experimental polymers are available within most individual polymer families. This limited coverage prevents statistically reliable class-wise comparisons. Therefore, we focus on global trends and overall model behavior rather than drawing conclusions about family-specific MD discrepancies.

Motivated by the systematic and largely global overestimation observed in MD-calculated  $C_{\text{p}}$  values, we examined a simple empirical bias-correction as a diagnostic analysis. Specifically, MD-predicted  $C_{\text{p}}$  values were linearly mapped onto the experimental scale using polymers common to both datasets according to

$$C_{\text{p}}^{\text{exp}} = aC_{\text{p}}^{\text{MD}} + b, \quad (7)$$

where the coefficients  $a$  and  $b$  were obtained from a least-squares fit to the overlapping MD-experimental subset. This linear mapping primarily removes the dominant mean shift associated with missing quantum suppression of high-frequency vibrational modes in classical MD simulations. The resulting bias-corrected MD values illustrate that the systematic offset in MD-calculated  $C_{\text{p}}$  can be reduced in principle by a simple linear correction, as shown in Fig. 4c. Importantly, this bias-correction is included only as a representative, *post hoc* diagnostic to demonstrate the nature and correctability of the MD bias. Bias-corrected MD values are not used to generate

training labels, to pretrain models, or to fine-tune or evaluate the transfer-learning framework. All reported transfer-learning results are obtained by pretraining on raw low-fidelity labels (MD or GC) and subsequently fine-tuning using experimental data only.

Similarly, the accuracy of the  $C_{\text{p}}$  values estimated using the GC method was evaluated by comparing them with experimental data. Fig. 4d presents the parity plot between GC predictions and experimental values. The GC method yields a moderately accurate estimation, with a coefficient of determination ( $R^2$ ) of 0.416. In contrast to the MD results, the GC predictions tend to slightly underestimate  $C_{\text{p}}$ , as indicated by a negative ME of  $-132.01 \text{ J (kgK)}^{-1}$ . This underestimation is likely due to the simplified additive nature of the GC method, which neglects long-range intermolecular interactions, conformational flexibility, and cooperative effects that are inherently present in experimental systems.<sup>51</sup> These phenomena can contribute to enhanced heat capacity values, but are not captured in the GC framework. Despite these limitations, a notable advantage of the GC approach is its computational efficiency. It does not require expensive molecular simulations and allows for rapid estimation of  $C_{\text{p}}$  values directly from SMILES representations. This makes GC attractive for generating large-scale datasets for data-driven modeling.

To evaluate the utility of simulation-generated data, we employed a TL strategy using multiple ML models trained on MD- and GC-derived  $C_{\text{p}}$  values. In this work, experimentally measured  $C_{\text{p}}$  values are treated as the highest-fidelity data and serve as the sole reference for model evaluation and fine-tuning. Both MD-derived and GC-derived  $C_{\text{p}}$  values are used as lower-fidelity proxy data; however, they do not form a strict linear fidelity hierarchy. Instead, they represent distinct approximation pathways with different bias and noise characteristics. The models tested include MLP, vanilla GNN (GIN and GCN), and GRE. Fig. 1 illustrates the TL workflow, where models are first pretrained on either MD- or GC-derived  $C_{\text{p}}$  data and then fine-tuned using the experimental dataset. The detailed implementation of the TL framework is described in the Methodology section. A nested cross-validation scheme with 5 outer folds and 3 inner folds was employed to obtain an unbiased estimate of model performance while optimizing hyperparameters. In each outer iteration, one fold was held out for testing, while the remaining data were used in a 3-fold inner loop to tune MLP hyperparameters based on validation loss with early stopping. Final performance metrics were computed by pooling predictions from all outer test folds, with fold-wise mean and standard deviation reported to quantify variability across splits. Table 1 summarizes the performance of different TL models after pretraining on either MD or GC datasets and fine-tuning on experimental data. Multiple molecular fingerprints were used to represent polymer structures for MLP models, while graph-based models were trained on molecular graphs with or without fingerprint augmentation. The results in Table 1 correspond exclusively to TL models. Performance metrics are reported as mean  $\pm$  standard deviation across the 5 folds.



Initially, we evaluated MLP models using six different molecular fingerprinting methods: Atom Pair, RDKit, Morgan, Polymer Embedding (PE), Topological Torsion, and MACCS fingerprints. In addition to the fingerprint vectors, a set of eight molecular descriptors was appended to the input features to improve model accuracy. These descriptors include Molecular Weight (MolWt), Topological Polar Surface Area (TPSA), Number of Hydrogen Bond Donors (NumHDonors), Number of Hydrogen Bond Acceptors (NumHAcceptors), Number of Rotatable Bonds, Ring Count, and Fraction of sp<sup>3</sup> Carbon Atoms (FractionCSP3). We observed that the impact of incorporating molecular descriptors was fingerprint-dependent, with some representations improving model performance while others led to marginal degradation. Each fingerprint was tested independently, and the results are shown in Table 1. In parallel, we also developed graph-based models, specifically GNN and GREA, which were trained directly on molecular graph representations of the polymers. In addition to the intrinsic graph features, we augmented the input with pre-computed molecular fingerprints such as Morgan and MACCS, as well as their combined representation. This approach allows the models to exploit not only the atom- and bond-level information captured by the molecular graph, but also complementary global descriptors that encode connectivity patterns and functional group presence.

To establish a fair benchmark, we trained the same model architectures directly on the limited experimental dataset without any pretraining. As shown in Fig. 5a, these direct-training models exhibited lower performance and higher variance, likely due to overfitting caused by the small sample size. In contrast, TL models pretrained on either MD or GC data and fine-tuned with experimental data demonstrated significantly improved performance. TL models pretrained on either MD or GC data and fine-tuned with experimental data demonstrated clear performance gains. Based on reductions in mean absolute error (MAE), the MD-based TL model reduced prediction error by 20.5% relative to the experimental-only model, while the GC-based TL model achieved a larger reduction of 23.8%. Additionally, the variance across five folds was noticeably reduced, indicating improved model robustness. The parity plots for the best-performing TL models using MD and GC data are shown in Fig. 5b and c, respectively. Although the experimental dataset spans diverse polymer families, the number of samples per family is small and uneven, and several polymers belong to multiple classes. This limits the statistical reliability of family-resolved comparisons and prevents robust conclusions about class-specific advantages of MD- versus GC-based TL. Accordingly, this study focuses on global trends and model-level behavior rather than family-specific claims. Within this scope, neither proxy is universally superior: GC-based pretraining offers broader chemical coverage and lower noise, whereas MD-based pretraining incorporates richer physical information but exhibits systematic bias that must be corrected during fine-tuning.

To assess generalization beyond random splits, we performed an additional stress test using a polymer-family

holdout strategy. The experimental dataset was grouped into five coarse classes based on backbone chemistry: (i) polyacrylics and polyvinyls, (ii) polyesters and thioesters, (iii) polyoxides, ethers, and acetals, (iv) polyamides, imides, imines, and urethane-based polymers, and (v) hydrocarbon and specialty polymers, including polyolefins, halogenated, sulfur-containing, and siloxane systems. Each group was held out in turn as an unseen test set, while the remaining groups were used for training and validation, with hyperparameters selected using a three-fold inner cross-validation loop. The resulting metrics, reported in Table 1, correspond exclusively to TL models pretrained on low-fidelity MD or GC data and fine-tuned on experimental data. Performance under polymer-family holdout is slightly lower than that obtained with random nested cross-validation, as expected for a chemically structured split, but remains stable across all folds. This indicates that the TL framework can generalize across distinct polymer families within the available experimental domain, while acknowledging that the evaluation remains within-domain rather than fully external.

To utilize the complementary strengths of the GC-based and MD-based predictive models, we examined simple ensemble strategies that combine their respective predictions. When evaluated individually, the GC-TL and MD-TL models exhibit comparable performance, with cross-validated  $R^2$  values of approximately 0.59 and 0.60, respectively. This indicates that neither model provides uniformly superior  $C_p$  predictions across the polymer chemical space. For each polymer in the experimental dataset, two independent  $C_p$  predictions were obtained, one from the GC-based model and one from the MD-based model. We then considered a simple arithmetic averaging of these predictions. Despite its simplicity, this ensemble approach consistently outperformed both individual models, achieving a pooled cross-validated  $R^2$  of 0.65. The observed improvement suggests that the GC and MD models capture partially complementary information and that averaging effectively mitigates model-specific bias and variance. The parity plot corresponding to the averaged GC and MD predictions is shown in Fig. 5d, where improved agreement with experimental  $C_p$  values is evident relative to the individual models. A comparison of prediction errors based on MAE for the experiment-only model, GC-TL, MD-TL, and the averaged ensemble is provided in Fig. 5e. For completeness, we also evaluated an idealized upper bound in which, for each polymer, the prediction closer to the experimental  $C_p$  value was selected between the GC and MD models. This oracle selection yields a higher  $R^2$  of 0.74, indicating that significant complementarity exists between the two models. While this approach is not deployable in practice due to its reliance on experimental values, it provides a useful reference for the maximum achievable performance attainable through optimal model combination.

Having established the performance of domain-specific ML models under the multi-fidelity TL framework, we next examine the applicability of recent general-purpose LLMs to polymer  $C_p$  prediction. This analysis is not intended to posi-



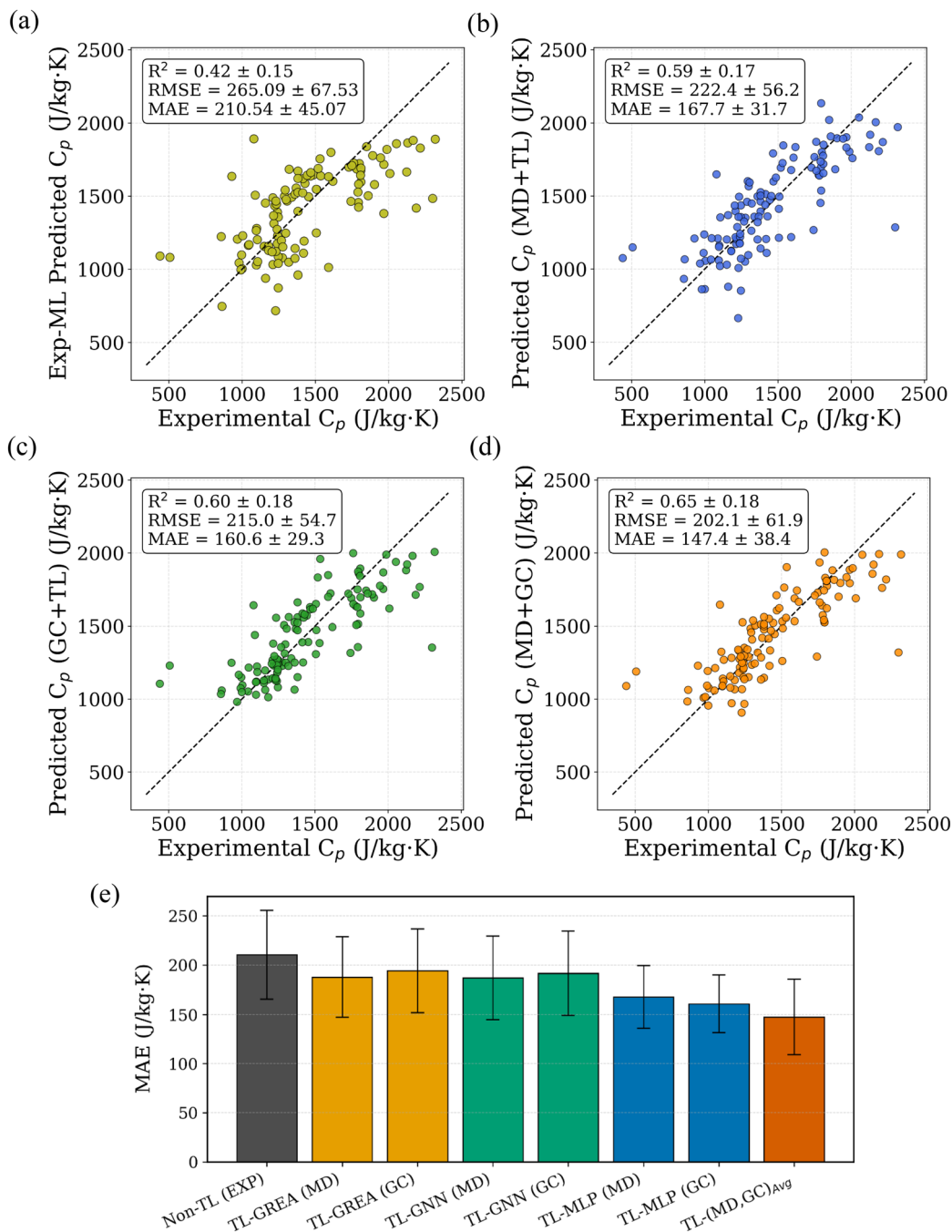


**Fig. 5** Evaluation of model performance using experimental data alone and with transfer learning (TL). (a) Parity plot of predicted vs. experimental  $C_p$  for the model trained only on experimental data. (b) TL model fine-tuned on experimental data after pretraining on the MD dataset (MLP + PE). (c) TL model fine-tuned on experimental data after pretraining on the GC dataset (MLP + AtomPair). (d) Parity plot for the averaged GC-MD ensemble, where predicted  $C_p$  values are obtained by simple arithmetic averaging. (e) Comparison of MAE across different model architectures and TL strategies.

tion LLMs as competitive quantitative predictors, but rather to assess their current limitations for numerical regression tasks in polymer science without task-specific training. The models evaluated include Llama 4, Qwen 3, GPT-4o, Gemini 2.0 Flash, and Mistral Large. These LLMs were used in an inference-only setting and were not fine-tuned on molecular property data,

allowing us to probe whether implicit chemical knowledge alone is sufficient for quantitative prediction. A cross-validation-based data partitioning scheme was employed in which the experimental dataset was split into multiple folds. Few-shot prompts were constructed exclusively from polymers in the training portion of each split, while predictions were evalu-



ated on the corresponding held-out data, preventing target information leakage and enabling fair comparison across models and prompting strategies. We examined multiple prompting configurations under both zero-shot and few-shot settings using 0, 5, 10, and 15 ICL examples, as well as different input representations, including SMILES strings, polymer IUPAC names, functional group descriptors, and their combinations. As summarized in Table 2, all tested LLM configurations perform substantially worse than traditional ML models, with several yielding negative  $R^2$  values. These results indicate that current LLM-based approaches lack the numerical accuracy required for quantitative polymer property prediction and should be interpreted strictly as exploratory or qualitative baselines.

Among the LLMs tested, Qwen3 produced the most accurate predictions. Notably, the inclusion of few-shot examples in the prompt improved model performance compared to zero-shot settings, and accuracy generally increased with the number of examples provided. Furthermore, supplementing the SMILES input with corresponding IUPAC names consistently enhanced predictive performance. Across all evaluated LLMs and prompting settings, SMILES-only prompts consistently yielded lower predictive accuracy than prompts combining SMILES with IUPAC names, indicating that the absence of name-based contextual information degrades LLM performance.

Despite these relative improvements, the accuracy of LLM-based predictions remains substantially lower than that of the specialized ML models considered in this work. In several cases, certain LLMs (e.g., GPT-4o) yield negative  $R^2$  values, indicating performance worse than a simple mean predictor. Accordingly, LLMs are not intended to serve as competitive predictors of polymer  $C_p$ , but are included as an exploratory baseline to assess whether general-purpose language models can extract coarse structure–property signals directly from polymer representations. The limited performance of LLMs in this setting can be attributed to the possibility of lack of chemical inductive bias, the absence of explicit exposure to

thermophysical property data such as  $C_p$  during pretraining, and their reliance on syntactic molecular encodings (e.g., SMILES) rather than physically informed molecular descriptors or graphs. As a result, their utility in the present context is qualitative and comparative rather than predictive. Overall, these results highlight the current limitations of LLMs for quantitative polymer property prediction and clarify their appropriate role relative to domain-specific ML models.

The next step in our study involved predicting  $C_p$  of polymers using the trained ML models. We predicted  $C_p$  values of 13 000 real polymer from PolyInfo database. The distribution of these predictions is shown in Fig. 6a. The predicted  $C_p$  values range from 298.17 to 2048.61 J (kgK)<sup>-1</sup>, with the majority of polymers exhibiting values clustered within the 1000–1200 J (kg K)<sup>-1</sup> range.

To expand the chemical space, we further applied the ML models to the PI1M database, which contains 1 million virtual polymer SMILES. The distribution of the predicted  $C_p$  values for this dataset is shown in Fig. 6b. The predicted values range from 106.89 to 3245.39 J (kg K)<sup>-1</sup>, with the majority of polymers clustered within the 1200–1500 J (kg K)<sup>-1</sup> range. Notably, the PI1M predictions span a broader  $C_p$  range compared to those from PolyInfo, suggesting the presence of novel structural motifs with potentially extreme thermal behaviors not captured in existing experimental databases. These large-scale predictions demonstrate the feasibility of using ML models to rapidly screen polymer candidates for desirable thermal properties, significantly accelerating the materials discovery process without the need for costly simulations or experimental measurements.

To better understand how molecular structure influences  $C_p$  in polymers, we analyzed the correlation between predicted  $C_p$  values and a set of structural and physicochemical descriptors. The descriptors considered include molecular weight, number of rotatable bonds, topological polar surface area, fraction of sp<sup>3</sup> hybridized carbons (as a proxy for backbone flexibility), heavy atom count, molar refractivity, ring count, and

**Table 2** Comparison of different LLM models for polymer  $C_p$  prediction using various identifiers and shot settings

Model	# Shots	Identifier	$R^2$	RMSE	MAE
Llama 4	5	SMILES	0.244 ± 0.24	346.44 ± 96.49	237.28 ± 68.99
Qwen3	5	<b>SMILES</b>	<b>0.296 ± 0.23</b>	<b>322.09 ± 7.43</b>	<b>206.36 ± 13.12</b>
GPT-4o	5	SMILES	-0.07 ± 0.35	399.11 ± 44.76	269.15 ± 28.59
Gemini 2.0 Flash	5	SMILES	0.264 ± 0.24	339.66 ± 80.08	241.95 ± 53.24
Mistral Large	5	SMILES	0.111 ± 0.23	372.83 ± 77.36	267.24 ± 50.76
Qwen3	0	SMILES	-0.622 ± 0.72	484.01 ± 109.79	396.47 ± 113.80
	5	SMILES	0.296 ± 0.23	322.09 ± 7.43	206.36 ± 13.12
	10	SMILES	0.348 ± 0.15	321.99 ± 72.45	223.52 ± 49.86
	15	<b>SMILES</b>	<b>0.397 ± 0.15</b>	<b>308.36 ± 64.69</b>	<b>204.99 ± 39.63</b>
Qwen3	5	SMILES	0.296 ± 0.23	322.09 ± 7.43	206.36 ± 13.12
	5	<b>SMILES + names</b>	<b>0.337 ± 0.16</b>	<b>315.99 ± 24.75</b>	<b>207.87 ± 18.68</b>
	5	SMILES + group	0.327 ± 0.13	321.24 ± 38.62	223.34 ± 36.08

Metrics are reported as mean ± standard deviation. Best results in each column are highlighted in bold.





Fig. 6 Histogram of ML-predicted  $C_p$  values for polymers in two datasets. (a) Predicted  $C_p$  distribution for over 13 000 polymers from the PolyInfo database. (b) Predicted  $C_p$  distribution for 1 million virtual polymers from the PI1M dataset.



Fig. 7 Correlation between predicted  $C_p$  values and various molecular descriptors for the PolyInfo dataset ( $N \approx 13\,000$  polymers): (a) molecular weight, (b) number of rotatable bonds, (c) topological polar surface area, (d) fraction of  $sp^3$  carbons, (e) heavy atom count, (f) molar refractivity, (g) ring count, and (h) number of hydrogen bond acceptors. Each scatter plot includes the corresponding Pearson correlation coefficient.

the number of hydrogen bond acceptors. The scatter plots of  $C_p$  versus each descriptor, along with their respective Pearson correlation coefficients, are shown in Fig. 7a–h.

The Debye model provides a theoretical basis for estimating the volumetric heat capacity at constant volume:<sup>52</sup>

$$C_v(T) = 9nk_B \left(\frac{T}{\theta_D}\right)^3 \int_0^{\theta_D/T} \frac{x^4 e^x}{(e^x - 1)^2} dx, \quad (8)$$

where  $n$  is the atomic number density,  $k_B$  is the Boltzmann constant,  $\theta_D$  is the Debye temperature, and  $T$  is the absolute

temperature. At temperatures much higher than  $\theta_D$ , this expression approaches the classical limit:

$$C_v \approx 3nk_B, \quad (9)$$

which represents three thermally accessible vibrational degrees of freedom per atom. In polymers, many high-frequency bond vibrations, especially those involving C–H or C=O stretching, are not excited at room temperature. The effective number of thermally active modes  $f_{\text{eff}}$  is therefore smaller than the classical limit of  $3n$ .



For condensed polymer solids, the difference between  $C_p$  and  $C_v$  is negligible because  $C_p - C_v = \alpha^2 BVT \ll C_p$ , where  $\alpha$  is the thermal expansion coefficient,  $B$  the bulk modulus,  $V$  the molar volume, and  $T$  the temperature.<sup>52</sup> Xie *et al.*<sup>53</sup> proposed a modified form of the Debye expression for amorphous polymers by reducing the effective atomic density to exclude hydrogen atoms that contribute only to high-frequency modes:

$$C_p \approx 3n_C k_B = 2(n - n_H)k_B, \quad (10)$$

where  $n_H$  is the number density of hydrogen atoms and  $n_C$  is the adjusted density of thermally active atoms. This model reproduces experimental  $C_p$  values of amorphous polymers with approximately 20% accuracy and emphasizes that the main contribution to  $C_p$  at 298 K arises from low-frequency torsional, skeletal, and conformational vibrations.<sup>54</sup>

Among all descriptors, the fraction of  $sp^3$  carbons shows the strongest positive correlation with  $C_p$  ( $r = +0.82$ ), confirming that flexible single-bonded carbon frameworks enhance the density of low-frequency modes.<sup>55</sup> The number of rotatable bonds also shows a positive correlation ( $r = +0.36$ ), indicating that torsional flexibility contributes to higher  $C_p$  through low-frequency modes, whereas ring count exhibits a negative correlation ( $r = -0.52$ ) because cyclic and aromatic structures restrict conformational motion and increase local stiffness.<sup>56</sup> Other descriptors, such as molecular weight, TPSA, heavy atom count, molar refractivity, and hydrogen bond acceptors, show weaker negative correlations ( $r = -0.25$  to  $-0.30$ ). Although heavier atoms tend to lower individual bond vibrational frequencies, their incorporation is often accompanied by bulkier or more rigid substituents that suppress accessible low-frequency modes.<sup>56</sup> Similarly, higher TPSA and larger numbers of hydrogen bond acceptors correspond to polar groups that form strong intermolecular interactions and further limit structural flexibility.<sup>56</sup> These effects collectively reduce the number of thermally active degrees of freedom  $f_{\text{eff}}$ , leading to lower  $C_p$ . Therefore, polymers with greater conformational flexibility exhibit higher  $C_p$  values, whereas rigid frameworks have lower heat capacities due to fewer accessible vibrational modes.

While ML-based models provide accurate  $C_p$  predictions, classical GC methods remain attractive due to their simplicity

and scalability. To improve the quantitative accuracy of GC-based  $C_p$  estimation, we next introduce a data-driven refitting strategy that leverages large-scale predicted datasets to update the GC parameters. The methodology leverages the predicted  $C_p$  values of 1 million polymers from the PI1M database, previously computed using our TL-based ML model. For each polymer, we extracted functional group counts from its molecular structure. These counts were then related to the corresponding predicted  $C_p$  (in  $\text{J mol}^{-1} \text{K}^{-1}$ ) using a non-negative least squares regression approach. The relation follows the standard additive GC framework:

$$C_p^{\text{molar}} = \sum_{i=1}^n N_i \cdot \text{GC}_i, \quad (11)$$

where  $C_p^{\text{molar}}$  is the molar  $C_p$  of the polymer,  $N_i$  is the number of occurrences of functional group  $i$ ,  $\text{GC}_i$  is the fitted contribution of group  $i$  to  $C_p$ , and  $n$  is the total number of functional groups considered. The regression was constrained to produce only non-negative GC values to maintain physical interpretability.

The regression analysis was performed using TL-predicted  $C_p$  values for 13 000 PolyInfo polymers and 1 million PI1M virtual polymers, and the resulting refitted GC values are reported in Table 3 alongside the original literature-based GC parameters (Sato formulation) as compiled by van Krevelen and te Nijenhuis<sup>39</sup> for direct comparison. To assess the performance of the newly proposed GC, we compared predicted  $C_p$  values against experimental values from the PolyInfo dataset. Fig. 8a shows the parity plot using the original literature-based GC values, which achieves an  $R^2$  value of 0.416. When recalculated using our newly fitted GC values derived from the 13 000 PolyInfo polymers, the  $R^2$  improves to 0.484 (Fig. 8b). The GC values fitted using the 1 million predicted PI1M data further enhance the correlation, yielding an  $R^2$  value of 0.562 (Fig. 8c), which corresponds to a 35% improvement over the original GC approach. The refitting procedure results in modest adjustments to the original literature-based GC values rather than introducing new functional groups or qualitative changes. Larger deviations are observed for certain halogen-containing groups (*e.g.*, Br and I), which are interpreted as empirical corrections arising from correlations

**Table 3** Comparison of original and refitted GC parameters for  $C_p$  at 298.15 K

Functional group	$C_p^{\text{Orig}}$	$C_p^{\text{Refit}}$	Functional group	$C_p^{\text{Orig}}$	$C_p^{\text{Refit}}$	Functional group	$C_p^{\text{Orig}}$	$C_p^{\text{Refit}}$
-CH <sub>3</sub>	30.90	35.54	-O-	16.80	25.98	-F	21.40	32.81
-CH <sub>2</sub>	25.35	25.35	-CO-	23.05	30.71	-Cl	27.10	27.10
>CH-	15.60	15.50	-COO-	46.00	53.37	-Br	26.30	78.24
>C<	6.20	6.20	-COOH	50.00	50.00	-I	22.40	140.45
=CH <sub>2</sub>	22.60	22.60	-OH	17.00	26.41	-CN	25.00	25.00
=CH-	18.65	27.70	-NO <sub>2</sub>	41.90	41.90	-CONH-	46.00	54.00
=C<	10.50	10.50	-NH <sub>2</sub>	20.95	20.94	-SO <sub>2</sub> -	50.00	49.72
-NH-	14.25	14.24	>N-	17.10	17.10	-SH	46.80	46.80
-S-	24.05	24.00	1-Sub benzene	85.60	92.00	2-Sub benzene	78.80	85.00
3-Sub benzene	65.00	80.00						

GC parameters are defined in molar units ( $\text{J mol}^{-1} \text{K}^{-1}$ ) following the Sato formulation as compiled by van Krevelen and te Nijenhuis.<sup>39</sup>





**Fig. 8** Comparison of GC model performance for  $C_p$  prediction: (a) using literature-based GC values, (b) using GC values fitted from 13 000 PolyInfo polymers, and (c) using GC values fitted from 1 million virtual polymers from P11M database.

present in the large predicted dataset rather than as physically fundamental constants. Because the refitted GC parameters are derived from model-predicted  $C_p$  values, they necessarily inherit uncertainties and biases associated with the underlying TL model. Accordingly, these parameters are not interpreted as intrinsic physical constants, but as data-driven corrections that improve empirical consistency with experimental trends within the scope of the available data. Further experimental measurements across chemically diverse polymers will be required to fully validate and refine these group contributions.

To extend the structural interpretation to the level of functional groups, we developed a separate tree-based regression model trained using functional-group occurrence counts as input features and the predicted polymer  $C_p$  values as targets. This approach captures how the presence of specific functional groups influences  $C_p$  across the dataset. The feature importance of this model was analyzed using the Shapley Additive Explanations (SHAP) method to quantify the direction and magnitude of each group's contribution (Fig. 9a and b).

Groups such as  $-\text{NH}-$ ,  $\text{CH}_3$ , and  $\text{CH}$  display positive SHAP values, indicating that their inclusion increases  $C_p$ . These structural motifs are associated with  $\text{sp}^3$  bonding and local torsional flexibility that enhances the density of low-frequency modes. In contrast, groups such as  $\text{C}=\text{O}$ ,  $=\text{CH}$ , aromatic rings, and  $-\text{OH}$  exhibit negative SHAP values, corresponding to their tendency to increase bond stiffness or restrict rotational motion. Halogen-containing groups show mixed behavior: heavier atoms such as  $\text{Cl}$  and  $\text{Br}$  yield small positive SHAP values, whereas strongly electronegative atoms such as  $\text{F}$  decrease  $C_p$ . The resulting SHAP hierarchy reproduces the same physical trend obtained from the descriptor analysis: chemical environments that promote soft, collective motions contribute positively to  $C_p$ , while those that introduce rigidity or strong electronic delocalization reduce it.

To qualitatively verify the SHAP-derived group ordering using an independent physical measure, we performed vibrational density of states (VDOS) analysis on a set of small molecules containing  $\text{CH}_3$ ,  $\text{CH}_2$ , and other representative functional groups (Fig. 10). The VDOS was obtained from the

Fourier transform of the mass-weighted velocity autocorrelation function (VACF). The velocity trajectories ( $v_x$ ,  $v_y$ ,  $v_z$ ) of all atoms were first extracted from the MD simulations. Prior to analysis, the overall translational and rotational (center-of-mass and rigid-body) motions were removed to isolate the intrinsic vibrational dynamics. Each atom  $i$  was assigned a mass-weighted velocity defined as

$$\mathbf{w}_i(t) = \sqrt{m_i} \mathbf{v}_i(t), \quad (12)$$

where  $m_i$  is the atomic mass and  $\mathbf{v}_i(t)$  is the instantaneous velocity vector. The mass-weighted VACF was computed as

$$C^{(m)}(\tau) = \sum_i \langle \mathbf{w}_i(0) \cdot \mathbf{w}_i(\tau) \rangle, \quad (13)$$

and subsequently normalized with respect to its zero-time value,

$$C_{\text{norm}}^{(m)}(\tau) = \frac{C^{(m)}(\tau)}{C^{(m)}(0)} = \frac{\sum_i \langle \mathbf{w}_i(0) \cdot \mathbf{w}_i(\tau) \rangle}{\sum_i \langle \mathbf{w}_i(0) \cdot \mathbf{w}_i(0) \rangle}. \quad (14)$$

The normalized VACF was then Fourier-transformed to obtain the VDOS,

$$g(\omega) = \int_0^\infty C_{\text{norm}}^{(m)}(\tau) e^{-i\omega\tau} d\tau, \quad (15)$$

where  $\omega$  is the angular frequency.<sup>37</sup>

The VDOS from different chemical groups indicates their contributions to the overall  $C_p$  (Fig. 10) shows the low-frequency spectral area ( $0\text{--}250\text{ cm}^{-1}$ ). The vibrational frequency corresponding to room temperature is approximately  $200\text{ cm}^{-1}$  based on the Bose–Einstein distribution. Therefore, we calculate the areas under the curve for different chemical groups in these studied cases. The integration window was extended to  $0\text{--}250\text{ cm}^{-1}$  to capture all relevant torsional and skeletal motions before the onset of higher-frequency stretching vibrations.<sup>56</sup>

Across all test molecules, the  $\text{CH}_3$  group consistently exhibits the largest integrated low-frequency area ( $A_{0\text{--}250}$ ), confirm-





**Fig. 9** (a) SHAP summary plot showing the distribution of SHAP values for each functional group across the dataset, where red and blue points represent high and low feature values, respectively. (b) Directional SHAP analysis showing the mean signed SHAP values for functional groups. Positive SHAP values (blue bars) indicate groups that increase  $C_p$ , whereas negative SHAP values (red bars) indicate groups that decrease  $C_p$ .



**Fig. 10** Vibrational density of states (VDOS) spectra obtained from molecular dynamics simulations after rigid-body motion removal and mass-weighted velocity correction. The low-frequency region ( $0-250 \text{ cm}^{-1}$ ) captures collective, torsional, and skeletal vibrations that dominate polymer heat capacity at ambient temperatures. Panels (a-f) show representative small-molecule fragments, comparing  $\text{CH}_3$  groups with selected functional groups from different chemical environments.



ing its strong association with soft torsional and skeletal vibrations. Functional groups such as C=O, aromatic, S, F, and Br display smaller  $A_{0-250}$  values compared to the CH<sub>3</sub> group within the same molecule, indicating comparatively stiffer local bonding and reduced accessibility of low-frequency modes. The only group that shows a comparable or slightly larger spectral area than CH<sub>3</sub> is -NH-. These observations generally align well with the SHAP ranking.

In addition to descriptor-based analysis, SHAP interpretation, and VDOS decomposition, we further examine local, atom-level contributions using the GREA model. Based on nested cross-validation, GREA is not the best-performing predictive model and is therefore used here primarily as a tool for interpretability. The central feature of GREA is its environment-based augmentation, in which atomic representations are conditioned on their surrounding chemical context. This allows the model to distinguish similar functional groups embedded in different environments and yields chemically meaningful atom-level attributions. The details of the GREA framework and its underlying formulation are described in the

original work by Liu *et al.*<sup>44</sup> Fig. 11 presents representative rationale visualizations for two high- $C_p$  polymers (Fig. 11a and b) and two low- $C_p$  polymers (Fig. 11c and d). Highlighted regions indicate atoms that contribute most strongly to the predicted  $C_p$ . For high- $C_p$  polymers, the model assigns greater importance to flexible aliphatic segments and heteroatom-containing linkages, which increase vibrational freedom and contribute to higher heat capacity. In contrast, low- $C_p$  polymers are characterized by rigid, highly fluorinated backbones and heavy halogen substitution, consistent with reduced vibrational freedom. Overall, these atom-level rationales provide localized and chemically intuitive confirmation of trends identified through descriptor analysis, SHAP values, and VDOS calculations, and help connect the model predictions to underlying physical mechanisms. These atom-level rationales should be interpreted as associative rather than causal. The highlighted contributions reflect correlations learned from the available training data between local chemical environments and predicted  $C_p$ , and do not imply direct mechanistic causation.



**Fig. 11** Representative GREA-based rationale visualizations illustrating structure–property attribution for polymer  $C_p$  prediction. Panels (a) and (b) show high- $C_p$  polymers, where the highlighted atoms correspond primarily to flexible aliphatic segments, ester linkages, and bulky substituents that promote enhanced vibrational freedom. Panels (c) and (d) show low- $C_p$  polymers, with attributions concentrated around rigid aromatic units, halogenated groups, and stiff backbone motifs associated with constrained molecular motion. Highlighted atoms indicate the top 30% of nodes ranked by model-derived importance.



With validated predictive models and a refined GC framework in place, we finally demonstrate how the predicted thermophysical properties can be used for application-oriented polymer screening and categorization. Using the ML-predicted  $C_p$  values, we identified promising polymer candidates for various thermal applications. Although the primary focus of this study is on  $C_p$ , selecting materials based solely on  $C_p$  is not sufficient for practical applications. As a demonstration of practical screening scenarios, we therefore incorporated two additional thermal properties, thermal conductivity (TC) and glass transition temperature ( $T_g$ ), sourced from our previous studies.<sup>9,13,28</sup> Table 4 provides a comprehensive overview of the categorization framework used. It includes: (i) the names of four application-specific polymer categories; (ii) threshold values for  $C_p$ , TC, and  $T_g$ , defined separately for the PolyInfo

dataset and for the larger PI1M database; (iii) functional descriptions outlining the role of each category; and (iv) representative example applications. Because PI1M contains a substantially larger and more diverse set of polymers, the corresponding thresholds were set at slightly higher values to reflect its broader property distribution. The threshold values for each property were chosen based on the distribution and upper-lower bounds of the TL-predicted values in each dataset, highlighting polymers with clearly distinct thermal behaviors. The application-oriented categorization presented here is intended as a high-level screening and prioritization framework rather than a device-level design or certification scheme. The  $C_p$ , TC, and  $T_g$  thresholds are defined heuristically to translate large-scale property predictions into application-relevant guidance, rather than as strict performance

**Table 4** Categorization of polymers based on thermal property thresholds, representative examples, and example applications

Category	Thresholds (PolyInfo)	Thresholds (PI1M)	Functional description	Example applications	Representative examples
Thermal interface materials (high $C_p$ , high TC, high $T_g$ )	$C_p \geq 1600$ $TC \geq 0.4$ $T_g \geq 100$ °C	$C_p \geq 1800$ $TC \geq 0.5$ $T_g \geq 130$ °C	Efficient heat transfer across interfaces with high thermal stability under operating conditions	Interface pads in CPUs/GPUs, power electronics, EV battery modules	High- $T_g$ engineering polymers (e.g., PEEK-like systems) used in thermally demanding structural applications
Thermal insulators (high $C_p$ , low TC, high $T_g$ )	$C_p \geq 1700$ $TC \leq 0.2$ $T_g \geq 120$ °C	$C_p \geq 2000$ $TC \leq 0.2$ $T_g \geq 110$ °C	Minimizes heat transfer while maintaining thermal and mechanical stability at elevated temperatures	Fire-resistant coatings, aerospace insulation, protective gear	Polyethylene-based materials exhibiting low TC and moderate-to-high $C_p$ under ambient conditions
Thermal buffers (high $C_p$ , low TC, low $T_g$ )	$C_p \geq 1800$ $TC \leq 0.2$ $T_g \leq 10$ °C	$C_p \geq 2200$ $TC \leq 0.2$ $T_g \leq -50$ °C	Acts as a thermal reservoir for energy absorption and damping at sub-ambient conditions	Cold chain packaging, biomedical storage, low-temperature wraps	HDPE and related polyolefins with low $T_g$ and strong thermal buffering behavior
Heat spreaders (low $C_p$ , high TC, high $T_g$ )	$C_p \leq 1000$ $TC \geq 0.4$ $T_g \geq 150$ °C	$C_p \leq 700$ $TC \geq 0.6$ $T_g \geq 150$ °C	Rapid dissipation of localized heat under high thermal loads and cycling	LED spreaders, aerospace electronics, laser cooling systems	Sulfur- and heteroatom-rich polymers reported to exhibit elevated TC and thermal robustness



**Fig. 12** Scatter plots of ML-predicted polymer properties in the  $C_p$ -TC- $T_g$  space. (a) Predictions for experimentally known polymers from the PolyInfo dataset ( $N = 13\,000$ ), categorized into four functional application classes. (b) Predictions for virtual polymers from the PI1M dataset ( $N = 1$  million), showing broader chemical diversity while following the same classification boundaries.



requirements. The selected threshold ranges are consistent with typical thermophysical property values reported for polymers in the literature. Mass-specific  $C_p$  of common polymers are generally reported in the range of approximately 1200–3000 J kg<sup>-1</sup> K<sup>-1</sup> at ambient conditions, while bulk polymer TCs typically lie between about 0.1 and 0.5 W m<sup>-1</sup> K<sup>-1</sup>.<sup>39</sup> Reported  $T_g$  span a broad range, from below room temp-

erature for flexible polymers to above 150–200 °C for thermally stable engineering polymers.<sup>39,57</sup> These literature-consistent ranges provide physical context for the heuristic thresholds adopted in Table 4.

We propose a categorization framework to link predicted thermal properties with application-specific needs. The thermal interface materials category targets applications



Fig. 13 Selected polymer candidates from the PolyInfo dataset representing four functional categories based on predicted  $C_p$ , TC, and  $T_g$ , with corresponding polymer class labels. Selection was based on threshold criteria from Table 4.



requiring efficient heat dissipation and structural stability, favoring polymers with high  $C_p$ , high TC, and high  $T_g$ .<sup>58</sup> Thermal insulators, commonly used in high-temperature environments, are characterized by high  $C_p$ , low TC, and high  $T_g$ , which minimize heat transfer.<sup>59</sup> Thermal buffers, relevant for energy storage or damping applications, require high  $C_p$ , low TC, and low  $T_g$  to provide thermal management at sub-ambient conditions.<sup>60</sup> Finally, we define heat spreaders as materials prioritizing rapid heat conduction and thermal resilience, requiring low  $C_p$ , high TC, and high  $T_g$ , which are ideal for high-performance electronics.<sup>61</sup> As a qualitative validation of the application-oriented categorization, we examine whether

well-known polymers are placed into categories consistent with their established thermophysical behavior reported in the literature. This comparison is intended to verify the physical plausibility of the screening framework rather than to serve as device-level validation. For example, polyethylene-based materials are widely used in applications where low TC and thermal buffering are desirable. High-density polyethylene (HDPE) exhibits mass-specific  $C_p$  in the range of approximately 1300–2400 J kg<sup>-1</sup> K<sup>-1</sup> and bulk TC on the order of 0.3–0.5 W m<sup>-1</sup> K<sup>-1</sup> at ambient conditions, together with a very low  $T_g$ .<sup>39</sup> These literature-reported properties satisfy the defining criteria of the low-conductivity categories in Table 4 (thermal insula-



**Fig. 14** Selected polymer candidates from the PI1M dataset representing four functional categories based on predicted  $C_p$ , TC, and  $T_g$ . Selection was based on threshold criteria from Table 4 with stricter cutoffs for this dataset.



tors/thermal buffers), consistent with the established use of polyethylene materials in insulating and thermal buffering roles. Similarly, high-performance engineering polymers such as poly(ether ether ketone) (PEEK), which exhibits a high  $T_g$  of approximately 143 °C and is commonly employed in thermally demanding environments requiring structural stability, are preferentially grouped into categories characterized by elevated  $T_g$  thresholds.<sup>39,57</sup> While PEEK is not selected for high thermal conductivity, its classification reflects the intended role of high- $T_g$  criteria in identifying thermally stable polymer classes. These examples demonstrate that the proposed threshold-based categorization recovers well-established qualitative distinctions among polymer classes, supporting its use as a first-pass screening and prioritization tool. The case studies show that ML models can quickly identify polymer candidates given property targets, and that this approach is generalizable to any custom-defined property targets.

Fig. 12a shows a scatter plot of the PolyInfo polymers, visualizing the relationship between  $C_p$ , TC, and  $T_g$ . The overlaid shaded regions indicate the approximate areas occupied by polymers with distinct combinations of thermal properties, corresponding to the four application categories discussed in Table 4. These regions highlight clusters of datapoints with relatively high or low values of  $C_p$ , TC, and  $T_g$ , representing typical candidates for applications such as thermal interface materials, insulators, buffers, and heat spreaders. Similarly, Fig. 12b presents the plot for the PI1M dataset. The same region boundaries are overlaid to visualize the distribution of newly screened polymers across the functional application space. With 1 million polymers, the PI1M dataset spans a larger chemical space, and since the threshold values are higher, it offers a selection of polymer candidates with more extreme properties.

Fig. 13 presents the selected polymer candidates from the PolyInfo database, with five representative polymers shown for each of the four application categories. Each polymer is depicted with its chemical structure, along with its polymer class, and corresponding thermal property values. For the selected polymers, the  $C_p$  values predicted using the ML model were cross-checked using the newly proposed GC method. For selection, only polymers where both ML-predicted and GC-derived  $C_p$  values satisfied the threshold criteria, defined in Table 4, were included. We adopted the GC method for  $C_p$  validation instead of MD simulations, as MD-predicted values tend to be systematically overestimated. This figure also illustrates the structural and thermal property diversity of representative polymers across four functional categories. In the Thermal Interface group, polyesters and polyphenylenes stand out with high values of  $C_p$ ,  $T_C$ , and  $T_g$ . The thermal insulator and buffer categories are mostly polyacrylics, polyolefins, and polyvinyls, which exhibit high  $C_p$  but low  $T_C$ , which are favorable for thermal resistance and energy absorption. Conversely, the heat spreader category includes polymers such as polysulfides and polyimines, which display relatively low  $C_p$  and high  $T_C$  and  $T_g$ , ideal for efficient heat spreading. These examples highlight real polymer candidates tailored for

specific thermal roles, reinforcing the utility of data-driven screening in materials design.

Similarly, Fig. 14 shows the selected polymer candidates from the P11M dataset, with five representative polymers displayed for each application category. The selections are based on the higher threshold values defined for P11M in Table 4. Each polymer is shown with its ML-predicted  $C_p$  value, along with the TC and  $T_g$ . Because the proposed application categories are derived from multiple predicted properties ( $C_p$ , TC, and  $T_g$ ), uncertainties from the individual predictive models may accumulate in the final classification. Accordingly, the resulting application labels should be interpreted probabilistically and used for candidate prioritization rather than definitive assignment. In addition, we verified that modest variations (on the order of  $\pm 10\%$ ) in the threshold values for  $C_p$ , TC, and  $T_g$  do not qualitatively alter the overall distribution of polymers across application categories, indicating that the screening results are robust to small threshold perturbations. By leveraging both established and large-scale virtual datasets, we demonstrate the potential to discover high-performing candidates across a broad chemical space. These selected polymers provide a strong foundation for further computational or experimental evaluation and showcase the practical relevance of data-driven screening strategies in polymer thermal property design.

## Conclusion

This work presents a comprehensive TL framework for predicting the  $C_p$  of polymers, a key property for efficient thermal energy management in various applications. ML models were first pretrained using large datasets generated from MD simulations and GC method calculations, and then fine-tuned on experimental data to improve accuracy. Multiple ML models were evaluated, including MLP, GNN, and GREA architectures, using a range of molecular fingerprints and structural descriptors. MLP model with TL showed superior performance, highlighting the effectiveness of combining structural priors with experimental trends.

The trained models were applied to polymers from both known and virtual datasets to perform large-scale  $C_p$  screening. We further explored LLMs as few-shot, training-free baselines; however, their performance was substantially inferior to domain-specific ML models, limiting their applicability for quantitative property prediction. Structure–property analysis, supported by SHAP interpretation and VDOS analysis, revealed that polymers with a higher fraction of  $sp^3$ -hybridized carbons and more rotatable bonds tend to exhibit increased  $C_p$  values because enhanced vibrational flexibility increases the number of accessible low-frequency modes. These trends align with the theoretical understanding that a greater number of low-energy, thermally accessible vibrational DOF significantly contributes to  $C_p$  in polymers.

In addition, we proposed new GC values through data-driven regression, providing an interpretable and lightweight alternative for  $C_p$  estimation. Based on predicted  $C_p$ , along with TC and  $T_g$ , polymers were classified into four application-



relevant categories: thermal interface materials, insulators, buffers, and heat spreaders. Representative candidates were identified for each category, demonstrating the practical utility of the screening framework. Overall, this study demonstrates how integrating multi-fidelity data, ML, and interpretable modeling can accelerate polymer discovery. The framework is adaptable and can be extended to other thermophysical properties, offering a valuable tool for guiding the design of advanced materials for thermal energy applications.

## Conflicts of interest

There are no conflicts to declare.

## Data availability

All data and code supporting this study are publicly available. The complete implementation of the machine-learning workflows is provided at <https://github.com/sobinalosious/POLY-CP-TL>. The repository includes: (i) the curated experimental  $C_p$  dataset used for training and evaluation, with corresponding SMILES representations; (ii) the proxy datasets used for pretraining, including MD and GC derived  $C_p$  values; (iii) the full MD workflow used to compute  $C_p$ , including LAMMPS input scripts and Python post-processing codes for both EMD and NEMD methods; (iv) the GC calculation code and parameter tables used to estimate  $C_p$  from SMILES; (v) all scripts required to reproduce the results reported in Table 1, including nested cross-validation, Optuna-based hyperparameter optimization, pretraining, fine-tuning, and evaluation pipelines; (vi) the exact cross-validation splits, random seeds, and fold-wise optimal hyperparameters; and (vii) trained model weights for the best-performing configurations.

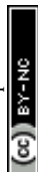
No human-subject or confidential data were used.

## Acknowledgements

This work was supported by the Lucy Family Institute for Data & Society Postdoctoral Fellowship and National Science Foundation grants 2332270, 2102592 and 2146761. The authors also acknowledge the Center for Research Computing at the University of Notre Dame for providing the necessary computing resources.

## References

- X. C. Tong, *Advanced Materials for Thermal Management of Electronic Packaging*, Springer, 2010, pp. 527–593.
- M. Sun, T. Liu, X. Wang, T. Liu, M. Li, G. Chen and D. Jiang, Roles of thermal energy storage technology for carbon neutrality, *Carbon Neutrality*, 2023, 2, 12.
- W. Wang, J. Ren, X. Yin, Y. Qiao and F. Cao, Energy-efficient operation of the thermal management system in electric vehicles via integrated model predictive control, *J. Power Sources*, 2024, 603, 234415.
- S. V. Garimella, T. Persoons, J. A. Weibel and V. Gektin, Electronics thermal management in information and communications technologies: Challenges and future directions, *IEEE Trans. Compon., Packag., Manuf. Technol.*, 2016, 7, 1191–1205.
- B. Lamrani, S. El Marbet, T.-u. Rehman and T. Kousksou, Comprehensive analysis of waste heat recovery and thermal energy storage integration in air conditioning systems, *Energy Convers. Manage.: X*, 2024, 24, 100708.
- A. R. Dhumal, A. P. Kulkarni and N. H. Ambhore, A comprehensive review on thermal management of electronic devices, *J. Eng. Appl. Sci.*, 2023, 70, 140.
- X. Zhang, Z. Li, L. Luo, Y. Fan and Z. Du, A review on thermal management of lithium-ion batteries for electric vehicles, *Energy*, 2022, 238, 121652.
- I. Sarbu and A. Dorca, Review on heat transfer analysis in thermal energy storage using latent heat storage systems and phase change materials, *Int. J. Energy Res.*, 2019, 43, 29–64.
- J. Xu and T. Luo, Unlocking enhanced thermal conductivity in polymer blends through active learning, *npj Comput. Mater.*, 2024, 10, 74.
- T. Zhang, X. Wu and T. Luo, Polymer nanofibers with outstanding thermal conductivity and thermal stability: fundamental linkage between molecular characteristics and macroscopic thermal properties, *J. Phys. Chem. C*, 2014, 118, 21148–21159.
- T. Luo, J. Garg, J. Shiomi, K. Esfarjani and G. Chen, Gallium arsenide thermal conductivity and optical phonon relaxation times from first-principles calculations, *Europhys. Lett.*, 2013, 101, 16001.
- L. Chen, H. Tran, R. Batra, C. Kim and R. Ramprasad, Machine learning models for the lattice thermal conductivity prediction of inorganic materials, *Comput. Mater. Sci.*, 2019, 170, 109155.
- R. Zhang, J. Xu, H. Zhang, G. Xu and T. Luo, Active learning-guided exploration of thermally conductive polymers under strain, *Digital Discovery*, 2025, 4, 812–823.
- X. Wei, Z. Wang, Z. Tian and T. Luo, Thermal transport in polymers: a review, *J. Heat Transfer*, 2021, 143, 072101.
- S. Kharbanda, T. Bhadury, G. Gupta, D. Fuloria, P. R. Pati, V. K. Mishra and A. Sharma, Polymer composites for thermal applications—A review, *Mater. Today: Proc.*, 2021, 47, 2839–2845.
- A. Henry, Thermal transport in polymers, *Annu. Rev. Heat Transfer*, 2014, 17, 485–520.
- M. Q. Le, J.-F. Capsal, J. Galineau, F. Ganet, X. Yin, M. Yang, J.-F. Chateaux, L. Renaud, C. Malhaire, P.-J. Cottinet, *et al.*, All-organic electrostrictive polymer composites with low driving electrical voltages for microfluidic pump applications, *Sci. Rep.*, 2015, 5, 11814.
- H. Luo, F. Wang, R. Guo, D. Zhang, G. He, S. Chen and Q. Wang, Progress on polymer dielectrics for electrostatic capacitors application, *Adv. Sci.*, 2022, 9, 2202438.



- 19 Y. Liu, S. Alosious, J. Zhou, M. Jiang and T. Luo, Machine Learning in Nanoscale Thermal Transport, *Annu. Rev. Heat Transfer*, 2025, **28**, 173–214.
- 20 M. O'Neill, Measurement of Specific Heat Functions by Differential Scanning Calorimetry., *Anal. Chem.*, 1966, **38**, 1331–1336.
- 21 R. Bhowmik, S. Sihn, V. Varshney, A. K. Roy and J. P. Vernon, Calculation of specific heat of polymers using molecular dynamics simulations, *Polymer*, 2019, **167**, 176–181.
- 22 Q. Waheed and O. Edholm, Quantum corrections to classical molecular dynamics simulations of water and ice, *J. Chem. Theory Comput.*, 2011, **7**, 2903–2909.
- 23 D. Rihani and L. Doraiswamy, Estimation of heat capacity of organic compounds from group contributions, *Ind. Eng. Chem. Fundam.*, 1965, **4**, 17–21.
- 24 R. Bhowmik, S. Sihn, R. Pachter and J. P. Vernon, Prediction of the specific heat of polymers from experimental data and machine learning methods, *Polymer*, 2021, **220**, 123558.
- 25 S. Alosious, M. Jiang and T. Luo, Computation and machine learning for materials: Past, present, and future perspectives, *MRS Bull.*, 2025, 1–13.
- 26 Y. Hayashi, J. Shiomi, J. Morikawa and R. Yoshida, RadonPy: automated physical property calculation using all-atom classical molecular dynamics simulations for polymer informatics, *npj Comput. Mater.*, 2022, **8**, 222.
- 27 I. P. Malashin, V. S. Tynchenko, V. A. Nelyub, A. S. Borodulin and A. P. Gantimurov, Estimation and prediction of the polymers' physical characteristics using the machine learning models, *Polymers*, 2023, **16**, 115.
- 28 R. Ma, H. Zhang, J. Xu, L. Sun, Y. Hayashi, R. Yoshida, J. Shiomi, J.-x. Wang and T. Luo, Machine learning-assisted exploration of thermally conductive polymers based on high-throughput molecular dynamics simulations, *Mater. Today Phys.*, 2022, **28**, 100850.
- 29 D. Weininger, SMILES, a chemical language and information system. 1. Introduction to methodology and encoding rules, *J. Chem. Inf. Comput. Sci.*, 1988, **28**, 31–36.
- 30 M. E. Fortunato and C. M. Colina, pysimm: A python package for simulation of molecular systems, *SoftwareX*, 2017, **6**, 7–12.
- 31 D. Vassetti, M. Pagliai and P. Procacci, Assessment of GAFF2 and OPLS-AA general force fields in combination with the water models TIP3P, SPCE, and OPC3 for the solvation free energy of druglike organic molecules, *J. Chem. Theory Comput.*, 2019, **15**, 1983–1995.
- 32 Y. Wu, B. Yao, X. Huang and Y. Chen, Integrating machine learning and molecular dynamics for accelerated discovery of polymers with high thermal conductivity, *J. Appl. Phys.*, 2025, **138**(17), 175101.
- 33 H. Yue, S. Wang, X. Sha and Q. Wang, Discovery of polymers with high bulk modulus and low thermal conductivity using a hybrid generative pipeline, *Chem. Eng. J.*, 2025, 164763.
- 34 S. Plimpton, Fast parallel algorithms for short-range molecular dynamics, *J. Comput. Phys.*, 1995, **117**, 1–19.
- 35 J.-P. Ryckaert, G. Ciccotti and H. J. Berendsen, Numerical integration of the cartesian equations of motion of a system with constraints: molecular dynamics of n-alkanes, *J. Comput. Phys.*, 1977, **23**, 327–341.
- 36 R. W. Hockney and J. W. Eastwood, *Computer simulation using particles*, CRC Press, 2021.
- 37 M. P. Allen and D. J. Tildesley, *Computer simulation of liquids*, Oxford University Press, 2017.
- 38 B. Jasiok, A. A. Pribylov, E. B. Postnikov, P. Friant-Michel and C. Millot, Thermophysical properties of the SPC/E model of water between 250 and 400 K at pressures up to 1000 MPa, *Fluid Phase Equilib.*, 2024, **584**, 114118.
- 39 D. W. Van Krevelen and K. Te Nijenhuis, *Properties of polymers: their correlation with chemical structure; their numerical estimation and prediction from additive group contributions*, Elsevier, 2009.
- 40 A. P. Bento, A. Hersey, E. Félix, G. Landrum, A. Gaulton, F. Atkinson, L. J. Bellis, M. De Veij and A. R. Leach, An open source chemical structure curation pipeline using RDKit, *J. Cheminf.*, 2020, **12**, 1–16.
- 41 R. Ma and T. Luo, PI1M: a benchmark database for polymer informatics, *J. Chem. Inf. Model.*, 2020, **60**, 4684–4690.
- 42 A. Gulli and S. Pal, *Deep learning with Keras*, Packt Publishing Ltd, 2017.
- 43 T. Akiba, S. Sano, T. Yanase, T. Ohta and M. Koyama, Proceedings of the 25th ACM SIGKDD international conference on knowledge discovery & data mining, 2019, pp. 2623–2631.
- 44 G. Liu, T. Zhao, J. Xu, T. Luo and M. Jiang, Proceedings of the 28th ACM SIGKDD Conference on Knowledge Discovery and Data Mining, 2022, pp. 1069–1078.
- 45 K. Xu, W. Hu, J. Leskovec and S. Jegelka, How powerful are graph neural networks?, *arXiv*, 2018, preprint, arXiv:1810.00826, DOI: [10.48550/1810.00826](https://doi.org/10.48550/1810.00826).
- 46 T. N. Kipf and M. Welling, Semi-supervised classification with graph convolutional networks, *arXiv*, 2016, preprint, arXiv:1609.02907, DOI: [10.48550/1609.02907](https://doi.org/10.48550/1609.02907).
- 47 D. Bajusz, A. Rácz and K. Héberger, Why is Tanimoto index an appropriate choice for fingerprint-based similarity calculations?, *J. Cheminf.*, 2015, **7**, 1–13.
- 48 S. Otsuka, I. Kuwajima, J. Hosoya, Y. Xu and M. Yamazaki, 2011 International Conference on Emerging Intelligent Data and Web Technologies, 2011, pp. 22–29.
- 49 D. A. McQuarrie, *Quantum chemistry*, University Science Books, 2008.
- 50 J. R. Lukes, D. Y. Li, X.-G. Liang and C.-L. Tien, Molecular Dynamics Study of Solid Thin-Film Thermal Conductivity, *J. Heat Transfer*, 2000, **122**, 536–543.
- 51 M. Rubinstein and R. H. Colby, *Polymer physics*, Oxford University Press, 2003.
- 52 C. Kittel and P. McEuen, *Introduction to solid state physics*, John Wiley & Sons, 2018.
- 53 X. Xie, K. Yang, D. Li, T.-H. Tsai, J. Shin, P. V. Braun and D. G. Cahill, High and low thermal conductivity of amorphous macromolecules, *Phys. Rev. B*, 2017, **95**, 035406.



- 54 B. Wunderlich and L. D. Jones, Heat capacities of solid polymers, *J. Macromol. Sci., Part B: Phys.*, 1969, **3**, 67–79.
- 55 A. Giri, C. J. Dionne and P. E. Hopkins, Atomic coordination dictates vibrational characteristics and thermal conductivity in amorphous carbon, *npj Comput. Mater.*, 2022, **8**, 55.
- 56 K. A. Bensley, R. V. Chimenti and S. E. Lofland, Low-Frequency Raman Spectroscopy of Polymers, *Macromol. Chem. Phys.*, 2025, 70004.
- 57 J. Bicerano, *Prediction of polymer properties*, CRC Press, 2002.
- 58 C.-P. Feng, L.-Y. Yang, J. Yang, L. Bai, R.-Y. Bao, Z.-Y. Liu, M.-B. Yang, H.-B. Lan and W. Yang, Recent advances in polymer-based thermal interface materials for thermal management: A mini-review, *Compos. Commun.*, 2020, **22**, 100528.
- 59 S. Cai, X. Deng, J. Beiyuan, X. Chen, D. Liu, D. Lv, C. Duan, L. Lin, R. Cha, W. Xie, H. Chen, J. Zhou, Z. Lu, L. Huang and W. Yuan, Review of synthetic polymer-based thermal insulation materials in construction and building, *J. Build. Eng.*, 2024, **97**, 110846.
- 60 Y. Jing, Z. Zhao, X. Cao, Q. Sun, Y. Yuan and T. Li, Ultraflexible, cost-effective and scalable polymer-based phase change composites via chemical cross-linking for wearable thermal management, *Nat. Commun.*, 2023, **14**, 8060.
- 61 C. Oshman, Q. Li, L.-A. Liew, R. Yang, Y. Lee, V. M. Bright, D. J. Sharar, N. R. Jankowski and B. C. Morgan, Thermal performance of a flat polymer heat pipe heat spreader under high acceleration, *J. Micromech. Microeng.*, 2012, **22**, 045018.

